

An indirect validation of convective heat transfer coefficients (CHTCs) for external building surfaces in an actual urban environment

Jiying Liu^{1,2}, Mohammad Heidarinejad^{3,4}, Stefan Gracik³, Jelena Srebric^{2,3,4} (✉), Nanyang Yu⁵

1. School of Thermal Engineering, Shandong Jianzhu University, Jinan 250101, China

2. Department of Architectural Engineering, The Pennsylvania State University, University Park, PA 16802, USA

3. Department of Mechanical Engineering, The Pennsylvania State University, University Park, PA 16802, USA

4. Department of Mechanical Engineering, University of Maryland, College Park, MD 20742, USA

5. School of Mechanical Engineering, Southwest Jiaotong University, Chengdu 610031, China

Abstract

The convective heat transfer is an important component in the estimation of thermal balance of energy for arrays of buildings immersed in a turbulent boundary layer. This study proposes a novel cost-effective validation approach using targeted field measurements and numerical simulations as an alternative to the wind-tunnel and full-scale field measurement approaches that typically require significant human resources and instrumentation to develop convective heat transfer coefficient (CHTC) for buildings located in the urban environment. This study first introduces new CHTC correlations for regular arrays of cubic buildings. A field measurement is then conducted in an actual urban thermal environment characterized by the plan area density $\lambda_p = 0.25$. Afterwards, this urban thermal environment is numerically simulated using CHTC values for the specified λ_p and appropriate thermal boundary conditions. The results of the numerical simulations are compared with the measured air temperatures to indirectly validate the CHTCs for external surfaces of buildings. The results show that the difference between the simulated and measured air temperatures is small and typically within 5%. Furthermore, this study created a calibrated building energy simulation model to deploy newly developed CHTCs for building heating energy consumption calculations. Specifically, the energy simulations used both newly developed and commonly used CHTCs to analyze the influence of CHTCs on the heating energy simulation results. A comparison between the simulated heating and actual heating energy consumption shows that the developed CHTCs have a positive influence on the accuracy of the energy simulation results.

1 Introduction

Urban environments are responsible for the changes in biogeochemical cycles and regional effects in the cities commonly known as the urban heat island (Grimm et al. 2008; Haghhighat and Mirzaei 2011; Kim and Kim 2011; Sarrat et al. 2006). Buildings located in the urban environment are one of the primary contributors to the changes in urban thermal, airflow, and air pollution patterns in the built environment (Hong and Lin 2014; Lin et al. 2008; Yamaoka

Keywords

CFD simulation,
convective heat transfer coefficients,
outdoor thermal environment,
field measurement,
energy consumption,
building energy simulation

Article History

Received: 12 August 2014

Revised: 22 December 2014

Accepted: 30 December 2014

© Tsinghua University Press and
Springer-Verlag Berlin Heidelberg
2015

et al. 2008; Zhao et al. 2008). The convective heat transfer coefficients (CHTCs) on external surfaces of a building are important parameters for accurate simulations of building thermal performance and associated building energy consumption. It has been shown that an uncertainty of 15% for CHTCs at external building surfaces can result in a corresponding uncertainty of 20% in the heat flux calculations through the building envelope (Wijeyesundara et al. 1993). Therefore, accurate predictions of CHTCs enable accurate calculations of the heat losses or gains at an external building

surface, allowing more accurate assessments of the air pollution dispersion and pedestrian thermal comfort in the built environment.

To obtain more accurate predictions of the CHTCs at the external surfaces of buildings, a large number of studies have been carried out by means of wind-tunnel experiments (Nakamura et al. 2001, 2003; Wang and Chiou 2006), numerical simulations (Blocken et al. 2009; Defraeye et al. 2010, 2011; Defraeye and Carmeliet 2010; Emmel et al. 2007), and field measurements (Clear et al. 2003; Hagishima and Tanimoto 2003; Liu and Harris 2007; Loveday and Taki 1996; Shao et al. 2009; Sharples 1984). However, the majority of the existing studies were limited to a building roof and/or vertical walls of a single isolated building, or to a certain location on a single building surface. In other words, existing CHTCs are not suitable for deployment to an entire neighborhood of buildings due to the complex building geometries and airflow patterns that are not all accounted for in the previous studies. It should be noted that the wind plays a significant role in the existing CHTC correlations, and the wind is strongly impacted by the buildings' surroundings as shown in building infiltration studies (Burley 2009; Mattingly and Peters 1977; Walker et al. 1996). Therefore, when estimating the CHTC values at the external building surfaces for an entire neighborhood, it is necessary to take into account the building surroundings. For example, the morphological parameters, such as the building plan area density (λ_p) and frontal area density (λ_f), have been shown to be important in predicting urban wind velocity profiles (Macdonald 2000). Here, λ_p is A_p/A_d and λ_f is A_f/A_d , where, A_p , A_f and A_d are the lot area, frontal area and plan area of obstacles, respectively, indicating the building density in urban areas.

Previously our studies developed and numerically validated a comprehensive set of CHTC correlations with the building plan area density (λ_p) for regular arrays of cubic buildings (Liu et al. 2014; Liu et al. 2013a). As a continuation of this prior work, the present study extends the application of the developed CHTC correlations to an actual urban neighborhood to enable validation of the CHTC correlations with the measured data and to demonstrate application of the developed CHTC correlations for energy modeling of an actual building located in an urban neighborhood.

2 Development of CHTC validation

The validation of the CHTCs at the external building surfaces with wind-tunnel and/or field measured data is an extension of the validation with different types of numerically simulated data (Liu et al. 2013a). The wind-tunnel experiments can enable estimates of not only the spatial single-point CHTCs,

but also the whole surface-averaged values of CHTCs (Meinders et al. 1997). However, most of the relevant wind-tunnel experiments focused on the convective heat transfer for the electronic equipment instead of being directly applied to building engineering and urban thermal environments (Nakamura et al. 2001, 2003). In addition, compared to buildings immersed in the atmospheric boundary layer with Reynolds numbers ranging from 7×10^5 to 7×10^7 (Liu et al. 2013a; Richmond-Bryant et al. 2011), electronic equipment components reside in a rather thin turbulent boundary layers with relatively low Reynolds numbers ranging from 2750 to 4970 (Meinders 1998). Therefore, these boundary conditions limit the applicability of the existing CHTCs for external building surfaces of an actual urban environment (Defraeye et al. 2011).

In the field measurements, the CHTCs can only be evaluated for specific locations on building enclosure, such as windows (Sharples 1984), rooftops (Clear et al. 2003) and vertical building walls (Liu and Harris 2007) due to typically enormous size and limited accessibility of these surfaces. Therefore, even though direct field measurements represent a dependable validation method, they can only be used for a limited number of locations on an external building surface. For surface-averaged CHTC distributions, field measurements could be unreliable due to limited number of discrete measurement locations (Shao et al. 2009), especially if all surfaces of a building need data for CHTCs. Overall, both wind-tunnel and field measurements require significant human resources and instrumentation. Therefore, this study proposes a novel indirect validation process to use measured outdoor air temperatures to compare to the calculated ones. This is an indirect validation process because accurate predictions of outdoor air temperatures indicate accurate convective heat fluxes resulting from CHTCs with measured surface temperatures for building enclosure boundary conditions.

3 Methodology

The main objective of this study is to validate the CHTC correlations using experimental data in an actual urban environment. These CHTC correlations were previously developed with Large Eddy Simulation (LES) simulation data for a three-dimensional regular array of buildings (Liu et al. 2013a).

3.1 Description of indirect validation workflow

The present study uses Reynolds Averaged Navier-Stokes (RANS) with a modified "Kato-Launder" version of the $k-\varepsilon$ turbulent (MMK) model to simulate urban thermal environment. A field measurement was conducted to provide

building wall temperatures and airflow field temperatures. Due to the safety regulations for campus buildings, the access to building roofs was not allowed during the measurement time period, as such, the heat balance equation was used to calculate the roof temperatures. The air temperatures obtained from the Computational Fluid Dynamic (CFD) simulations and field measurements were compared to indirectly validate the accuracy of CHTCs for external surfaces of buildings. As a final step, this study deploys the developed CHTC correlations into an energy simulation model for an actual building located in an urban neighborhood to demonstrate the importance of accurate calculations of heat losses or gains at the external building surfaces on the accuracy of the building heating energy consumption calculations. The results obtained with the developed CHTC correlations are then compared to the results obtained with the commonly used CHTC correlations in the literature as well as the metered heating energy consumption data. Figure 1 shows a detailed flow chart of the CHTC validation process for external building surfaces. Here, this study introduces relevant CHTC correlations, as well as the heat balance equations and a turbulence model. Note that the detailed descriptions of field measurement and CFD simulation setup for validation were separately provided in the Sections 5 and 6, respectively.

3.2 Convective heat transfer coefficient for regular arrays of buildings

CHTCs for five different building layouts characterized by plan area densities λ_p , including: 0.04, 0.063, 0.11, 0.16 and 0.25, were taken into account (Liu et al. 2013a). The CHTC values were correlated with the bulk wind speed, U_{10} , and λ_p

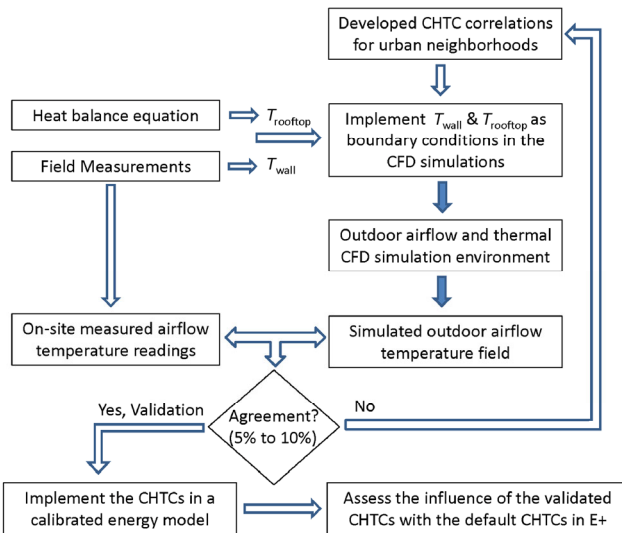


Fig. 1 Flow chart for validation of the CHTCs at external building surfaces

for windward, leeward, lateral, and top surfaces. The CHTC correlations were expressed by the following equation:

$$h_c = (a + b\lambda_p)U_{10}^c \quad (1)$$

where a , b and c are two coefficients and an exponent, respectively. Table 1 shows the values of correlation coefficients for different λ_p and U_{10} , where λ_p varies from 0.04 to 0.25 and the Reynolds number ranges from 7×10^5 to 5×10^6 . Detailed explanations on the variation of the CHTCs for different plan area density can be found in (Liu et al. 2013a).

Table 1 Convective heat transfer coefficient (h_c) correlations using the plan density λ_p and the incoming wind velocity at 10 m above the ground U_{10} for arrays of buildings

Surface	h_c for arrays of buildings ($0.04 \leq \lambda_p \leq 0.25$)
Windward	$(4.52 + 2.37\lambda_p)U_{10}^{0.79} (R^2 = 0.90)$
Leeward	$(2.40 + 1.69\lambda_p)U_{10}^{0.79} (R^2 = 0.89)$
Lateral	$(4.35 - 3.38\lambda_p)U_{10}^{0.79} (R^2 = 0.85)$
Top	$(4.28 + 1.81\lambda_p)U_{10}^{0.79} (R^2 = 0.88)$

3.3 Heat balance equation

In this study, the rooftop temperatures are calculated by the surface heat balance equation defined as follows:

$$Q_{abs} + Q_{long} + Q_{conv} + Q_{cond} + Q_{lat} = 0 \quad (2)$$

where Q_{abs} is the absorbed solar radiation, Q_{long} is the net longwave radiation, Q_{conv} is the convective heat transfer at the building wall, Q_{cond} is the conductive heat, and Q_{lat} is the latent heat transfer. Detailed equations for each heat flux can be found in the literature (Chen et al. 2004; Elnahas and Williamson 1997; Huang et al. 2005). Note that the rooftop temperature calculations assumed negligible window effects on CHTCs, uniform enclosure thermal properties for each side of the building, and a uniform temperature inside the building. An airport weather station near the field measurement site provided air temperature, relative humidity, solar radiation, and wind direction and velocity.

3.4 MMK turbulence model

The standard $k-\varepsilon$ turbulence model yields unsatisfactory prediction when applied to flow around bluff bodies in wind-engineering applications. The model fails to reproduce the surface pressure distribution around a bluff body because of the tendency to overestimate turbulent production in the impingement region on the frontal area of the body. Kato and Launder (Kato and Launder 1993) resolved the problem concerning the overestimation of turbulence kinetic energy

k by modifying the expression for the production rate of turbulence kinetic energy (P_k). However, the mathematical inconsistency in the modeling of Reynolds stresses $-\overline{u'_i u'_j}$ and P_k still exists. Tsuchiya et al. (1997) proposed a new revised “Kato-Launder” version of the $k-\epsilon$ turbulence model (MMK model), which corrected this inconsistency of the Kato and Launder model by adding the modification not to the expression for P_k , but to the expression for the eddy viscosity (ν_t). The model equation for expressions of P_k and ν_t are

$$P_k = \nu_t S^2 \quad (3)$$

$$\nu_t = C_\mu^* \frac{k}{\varepsilon}, \quad C_\mu^* = \frac{C_\mu \Omega}{S} (\Omega/S < 1) \quad (4)$$

$$\nu_t = C_\mu^* \frac{k}{\varepsilon}, \quad C_\mu^* = C_\mu (\Omega/S \geq 1) \quad (5)$$

where $C_\mu = 0.09$, S and Ω are strain and vorticity parameters, respectively, defined by

$$S = \sqrt{\frac{1}{2} \left(\frac{\partial U_i}{\partial x_j} + \frac{\partial U_j}{\partial x_i} \right)^2} \quad (6)$$

$$\Omega = \sqrt{\frac{1}{2} \left(\frac{\partial U_i}{\partial x_j} - \frac{\partial U_j}{\partial x_i} \right)^2} \quad (7)$$

The MMK model has been widely used to predict urban wind environments (Huang et al. 2007; Mochida and Lun 2008; Tominaga et al. 2008), and it was implemented in PHOENICS commercial software as an extension to the high-Reynolds number $k-\epsilon$ model (Davidovic et al. 2014; PHOENICS 2010). Therefore, this study applies this model to predict thermal environment in an actual urban area to indirectly validate the CHTCs on building enclosure.

4 Field measurements

The field measurement was conducted around four student dorms at the Pennsylvania State University campus from 11:00 to 15:00 on June 11, 2012. Figure 2 shows the building plans and layout for measurement locations of air temperatures. The wall temperatures for Buildings A, B, C, D, E, and the ground temperatures were measured every hour. This study also measured wall temperature for Building E even though this building only has the height of 3.5 m, because it is helpful for the building boundary condition setup. This short building interconnects the four student dorms. Air temperatures at four locations (Nos. 1, 2, 3 and 4) around the multiple buildings were collected at 2 m, 4 m, 6 m and 7 m above the ground. Due to the existing safety regulations for campus buildings, these four locations were selected based on existing lamp poles that provide support

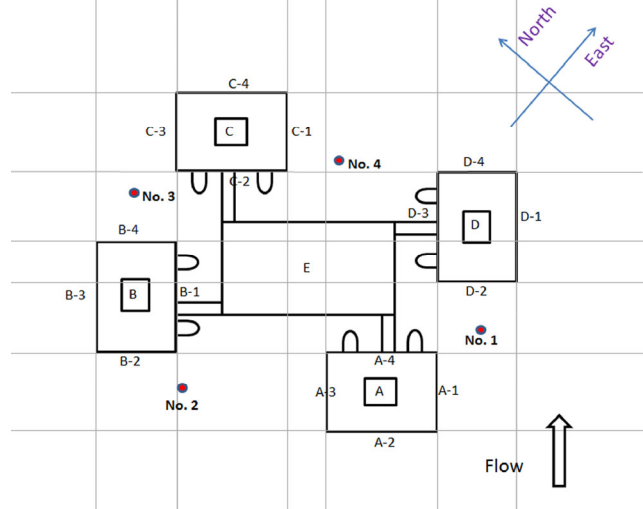


Fig. 2 Building plan and layout for measuring locations of air temperatures (Liu et al. 2013b)

with sufficient elevation. The meteorological data were obtained from the airport weather station that is 6 km away from the field measurement site (NOAA 2011).

4.1 Instrumentation

An infrared (IR) camera was used to measure the temperature at the building surfaces and ground. A previous study successfully used an IR camera to obtain the spatial temperature distribution on the surface of buildings and ground for assessment of the overall building heat transfer coefficient (Fokaides and Kalogirou 2011; Hoyano et al. 1999). This study uses an FLIR E40 camera with 160×120 pixels that can deliver temperature measurements with $<0.07^\circ\text{C}$ thermal sensitivity and 2% accuracy (FLIR Systems 2013). In addition, this camera works well in the longer wavelengths (8–14 μm), which is more appropriate for lower temperatures (0–100 $^\circ\text{C}$). This 3.1 MP camera provides the capability of having a standard visual light image and corresponding thermal image. Figure 3 shows the images of temperature distribution for four subzones of one vertical building wall (B-2).

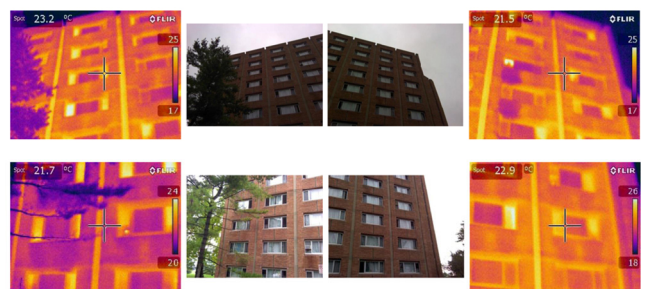


Fig. 3 Temperature distributions ($^\circ\text{C}$) for four subzones of one building vertical wall (B-2)

The mean emissivity value of 0.90 was selected for the infrared camera based on the physical properties of building walls and the ground. Note that in order to reduce measurement error, the IR camera was shaded to block the direct solar rays when capturing the thermal images. In addition, to attain a quasi-static thermal environment, it was necessary to finish the test in a relatively short time period. Specifically, as a handheld thermal imager, the camera operator took nearly 100 images for all the building walls and the ground in 10–15 minutes during every measuring time period. Due to restrictions and resultant potential errors for larger angle of gradient (Cehlin et al. 2002), all the measurements were completed with small enough angle of gradient of around 20° to 40° to collect accurate temperature data.

The DS1922L temperature logger iButton sensors were used to record the airflow field temperatures around the multiple buildings as shown in Fig. 4(a). This digital thermometer is a wireless temperature system with accuracy of $\pm 0.5^\circ\text{C}$ from -10°C to $+65^\circ\text{C}$ and with the precision of 0.0625°C (Maxim Integrated 2013). As found in previous research studies, this device is a convenient alternative to the conventional thermistors and thermocouples in those situations in which the wired thermal sensors are impractical and fast instrument responses are not critical (Lichtenbelt et al. 2006). For the past ten years, iButton sensors have been widely employed to measure human skin temperature, and then evaluate the thermal comfort in the HVAC research field (Hilmer et al. 2010; Lichtenbelt et al. 2006; Taylor et al. 2004). Only a few studies have used iButton sensors to measure airflow temperature in/around buildings (Fitzgerald et al. 2011; Holden et al. 2011). Since the iButton sensor is a computer chip enclosed in a 16 mm thick stainless steel enclosure, it is very sensitive to direct solar radiation. However, the existing studies did not account for a shading factor when recording the outdoor temperatures.

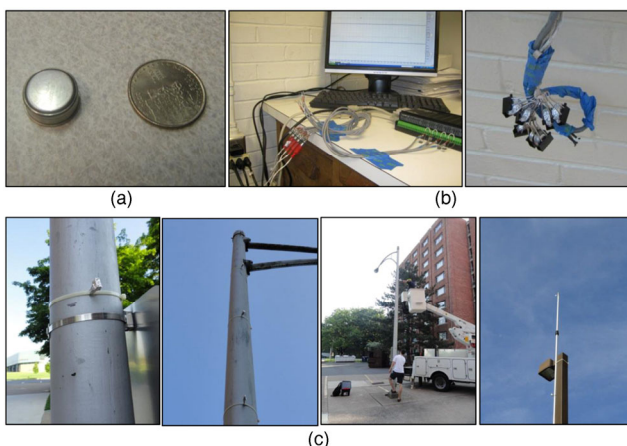


Fig. 4 Experiment details: (a) the iButton size comparison, (b) layout for validation test, and (c) in-situ iButton setup

In the present study, aluminum foil was used to cover the iButton sensors to shield it from the direct solar radiation. Aluminum foil has a high reflectivity and good conductivity, so it can enable iButton sensors to measure outdoor air temperatures.

To demonstrate the effect of aluminum foil protection on air temperature measurements with iButton sensors, a comparison test was carried out. Figure 4(b) shows a thermistor, protected iButton sensor and unprotected iButton sensor. The results showed that temperatures measured by the unprotected iButton sensor were higher than that of the protected iButton sensor and the thermistor as shown in Fig. 5. The difference was measured with the maximum value of 3.8°C . Furthermore, the results exhibited a good agreement between the data collected by the thermistor and protected iButton sensor. Therefore, protected iButton sensors, attached to street light poles, were used to collect outdoor air temperatures as shown in Fig. 4(c).

4.2 Measurement results for temperature distributions

Figure 6 shows area-averaged temperatures for the vertical building surfaces (A-1 to A-4, B-1 to B-4, C-1 to C-4 and D-1 to D-4) from 11:00 to 15:00 hours. The values for wall surface 1 at all buildings show higher temperatures than the temperatures at other wall surfaces, especially at 11:00 and noon. This effect is due to the fact that the wall surface 1 was exposed to the direct solar radiation for a longer period of time than the period of exposure any other building wall surface due to its south-east orientation. In the afternoon, the wall temperatures gradually decreased by about $6\text{--}7^\circ\text{C}$ until 15:00 hours. In contrast, wall surfaces 2, 3 and 4 were shaded from the direct solar radiation until 13:00 hours. Thereafter, the maximum temperatures for these wall surfaces did not exceed those for surface 1, even though

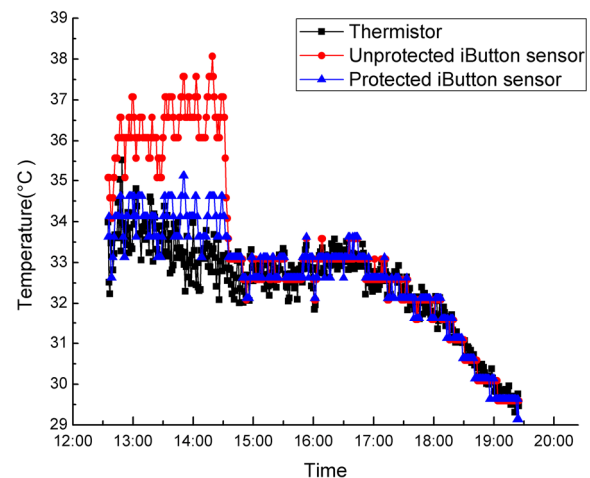


Fig. 5 Variation of temperature readings measured with thermistor, unprotected iButton sensor, and protected iButton sensor

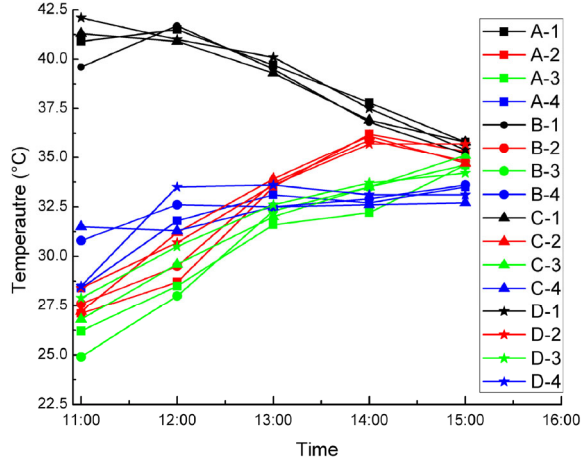


Fig. 6 Temperature changes for all vertical surfaces (A1–A4, B1–B4, C1–C4 and D1–D4) from 11:00 to 15:00 hours

wall surface 2 received a large amount of longwave radiation starting at 14:00 hours. In addition, the air temperatures from the weather station were 26°C at 11:00 hours, 26°C at 12:00 hours, 27.2°C at 13:00 hours, 27.2°C at 14:00 hours, and 26°C at 15:00 hours. A large difference between the surface temperatures and air temperatures indicated the presence of direct solar radiation. Furthermore, the surface temperature for the grass area exposed to the sun at 13:00

hours was 25°C to 31°C, and 25°C to 27°C in the shade. The surface temperature of concrete covered ground at 13:00 hours was 41°C to 46°C in the sunshine, and 37°C to 40°C in the shade.

Figure 7 shows airflow temperatures at different elevations for each location (Location No. 1, No. 2, No. 3 and No. 4) from 11:00 to 15:00 hours. The range of measured temperatures is from 28°C to 31°C in the entire measurement time period, except the time period at 10:45 when the temperature reached 33°C. Moreover, the measured temperatures changed at a relatively fast frequency of 5 minutes. This is due to the influence of the intermittent direct solar radiation because the weather on that day was slightly cloudy. Figure 7 also shows a smaller vertical temperature difference among the elevations of 2 m, 4 m and 6 m, in addition to Location No. 3 where the temperature difference between 2 m and 6 m was approximately up to 3.5°C. However, a very large temperature difference was not expected to occur in these locations. Note that the Reynolds number and Richardson number were 2.9×10^6 and 0.08, respectively. Therefore, the zone near the ground (2 m to 7 m) was intensively affected by airflow around the buildings instead of being affected by the air buoyancy effect close to the ground.

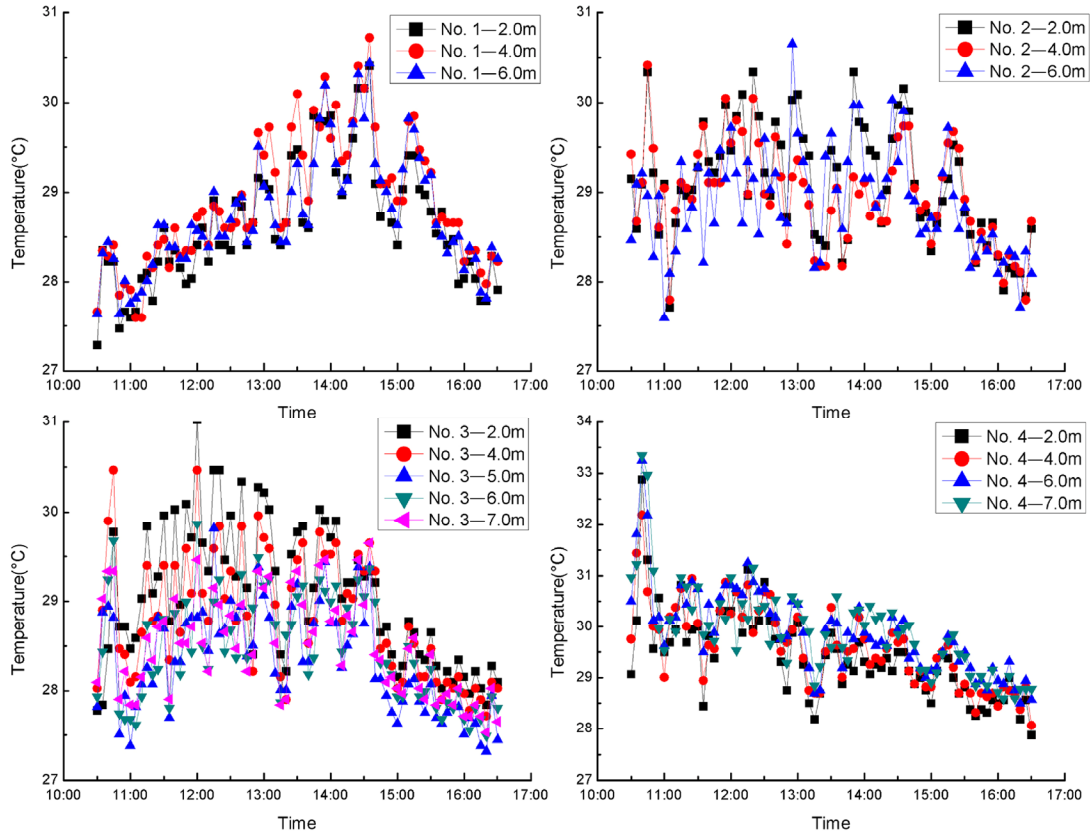


Fig. 7 Airflow temperatures at different elevation for each location (No. 1, No. 2, No. 3 and No. 4) from 11:00 to 15:00 hours

5 CFD simulation setup for validation

In the present study, an actual urban environment was modeled to indirectly validate the CHTC correlations using MMK turbulence model. This simulation setup includes building model and computational grids as well as the boundary conditions. Particularly important boundary conditions include ground surface cover with vegetation.

5.1 Descriptions of building model and computational grids

The building model includes four studied buildings and their surrounding environment. Figure 8(a) shows the aerial view of the studied site, and Fig. 8(b) presents the simulation model of the studied outdoor environment. The green blockages represent the vegetation model to be discussed in more detail below. According to the recommendations from previous studies (Franke et al. 2007), the distance between the inflow boundary and the first building was $5H$, and the distance between the outlet boundary and the last building in the domain was $15H$, where H is the averaged building height. In addition, the domain features a distance of $5H$ between the lateral boundary and the closest lateral building wall, and $5H$ between the top boundary of the domain and the closest top surface of a building.

A structured grid was employed in the entire computational domain. The grid independence evaluation was carried out by changing the grid distribution around buildings in all three directions. Three different grid distributions were arranged with $160 \times 150 \times 85$ (coarse mesh, Δ_1), $196 \times 180 \times 100$ (medium mesh, Δ_2), and $235 \times 216 \times 120$ (fine mesh, Δ_3). The surface-averaged skin friction coefficient (C_f) for the windward surface of Building A was compared for the various grid distributions. This quantitative grid verification was performed using the grid convergence index

(GCI) (Roache 1994) based on Richardson extrapolation (Franke et al. 2007). In this study, the GCI was described as $GCI[\text{fine}] = F_S|\varepsilon|/(r^p - 1)$, where $F_S = 1.25$ represents the safety factor when comparing three grids, ε is the relative error between coarse and fine grid solutions, and $p = 2$ is the order of the discretization method based on the second-order discretization of all terms in space (Hefny and Ooka 2009). The simulation results showed that $GCI[3,2] = 4.01\%$, and $GCI[2,1] = 9.52\%$. It was observed that a small value of GCI index occurred when comparing the medium and fine grid results. Therefore, a grid distribution of $(196 \times 180 \times 100)$ showed a good performance, resulting in a grid independent flow around cubes. This grid distribution provided a good compromise between the level of uncertainty and computational cost.

An important parameter for the mesh generation is the distance between the wall surfaces to the center of the first cell adjacent to the wall. This study relies on the recommendations in the literature to identify the range variation for the y^+ and maximum allowable y^+ in the simulations. Although it is stated in various studies that standard “logarithmic wall function” cannot provide an accurate representation of the convective heat transfer, especially for the natural convection (Awbi 1998; Murakami 1993), generalized logarithmic law wall functions are still widely used in the CFD simulations of urban thermal environments (Chang et al. 2004; Chen et al. 2009; Gromke et al. 2015; Hong and Lin 2015; Huang et al. 2005; Toparlar et al. 2015), in which the dimensionless parameter y^+ in the near-wall region obviously exceeded 30 and reached up to 300. A recent natural ventilation study showed a good agreement for the temperature distributions calculated with the standard wall function and enhanced wall function (Farea et al. 2015). Therefore, since the outdoor CFD simulations in this study are characterized by the forced convection, based on the recommendations in the literature, this study used the

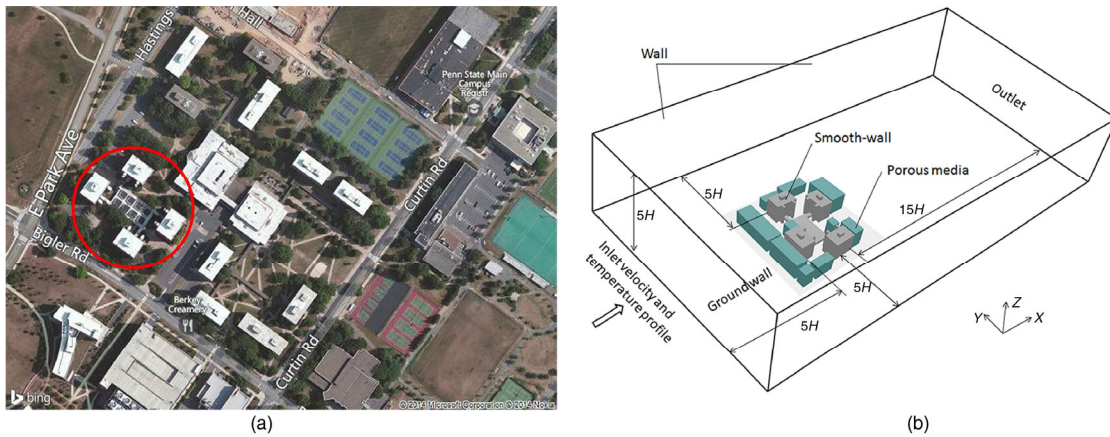


Fig. 8 (a) Aerial building neighborhood view and (b) computational domain, building and vegetation configuration model and boundary condition

generalized logarithmic law wall functions to simulate the flow field with the selected high-Reynolds turbulence model. Overall, the selected distance between the wall surfaces to the center of the first cell adjacent to the wall for the majority of the y^+ values were within the range of 30 to 100, while the maximum value was up to 200 in the high velocity region around building edges at the top building surface. Therefore, this study used less computational resources and facilitated the required simulations.

5.2 Boundary condition setting

This study uses the logarithmic wind profile at the inlet of the computational domain to represent the incoming wind velocity profile. Equations (9) and (10) show the definition of the turbulent kinetic energy (k) and the turbulent dissipation rates (ε).

$$\frac{U(z)}{u^*} = \frac{1}{\kappa} \ln\left(\frac{z + z_0}{z_0}\right) \quad (8)$$

$$k = \frac{u^{*2}}{0.3} \quad (9)$$

$$\varepsilon = \frac{u^{*3}}{k(z + z_0)} \quad (10)$$

where κ is the von Karman constant ($\kappa = 0.4$), u^* is the friction velocity and z_0 is the roughness length. This study uses z_0 of 0.3 as a representation of numerous short obstacles in small towns. U_{10} is the mean wind velocity at a height of 10 m above the ground. U_{10} was set to 5.0 m/s to reach the Reynolds number of 2.9×10^6 , based on the building height and U_{10} . The zero-gradient condition was used at the outlet boundary condition to generate a fully developed flow.

The development of inlet temperature profile boundary conditions for the non-isothermal simulations takes a few steps. This study first simulated target buildings with surrounding environment using the logarithmic velocity profile and isothermal temperature profile for the inlet to generate the initial boundary conditions. Second, the domain heat source is included to simulate the temperature field for the downstream air temperature profile. For the generation of the boundary conditions in the preliminary numerical simulation, wind attributes included open sky, ground plane, and SUN setting. This simulation method for generation of inlet temperature profiles was previously proposed and tested in the reference (Takahashi et al. 2004). These air temperature profiles provided good simulation results in the lowest 150 m of the atmospheric boundary layer (Oke 1987). Detailed descriptions of building layout and the non-isothermal air temperature profile for inlet boundary condition can be found in the literature (Liu et al. 2013b).

In the present study, the top and side surfaces of the domain were modeled as the non-free slip wall. The temperatures for top and side surfaces were assumed to have temperatures of 50°C and 40°C, respectively, based on the recommendations found in the literature (Takahashi et al. 2004). The ground surface of the domain was represented as the surface temperature boundary with zero roughness. The grass covered ground temperatures and concrete covered ground temperatures around the studied four buildings were averaged with the approximate values of 28°C and 44°C in the areas with the direct solar exposure, respectively, and with the approximate value of 26°C and 38°C in the shade, respectively. The temperature for the other areas of the ground had a constant value of 45°C. The temperatures for four building rooftops were calculated using the heat balance equation and the rooftop temperatures were set up to 49.6°C in the simulations (Liu et al. 2013b). This study represented the building walls as heated plates. Heat sources were applied to the building walls with specified convective heat transfer coefficients and the building wall temperatures. CHTC values for $\lambda_p = 0.25$ accounted for the actual urban density of the studied neighborhood.

5.3 Radiation model and vegetation effect

This study used the IMMERSOL radiation model (PHOENICS 2010) to describe the influences of heat conduction within the solids and the radiation in fluid domain between the solids. Since the field measurements provided the wall temperatures as the boundary conditions, this study only considered radiation in the fluid domain as follows:

$$\frac{\partial}{\partial x} \left(k \frac{\partial T_3}{\partial x} \right) + \frac{\partial}{\partial y} \left(k \frac{\partial T_3}{\partial y} \right) + \frac{\partial}{\partial z} \left(k \frac{\partial T_3}{\partial z} \right) = (\alpha + s)\sigma(T^4 - T_3^4) \quad (11)$$

where T_3 is the radiosity temperature of the fluid, T is the temperature of the fluid, α is the absorption coefficient of fluid, s is the scattering coefficient of fluid, σ is the Stefan-Boltzmann constant ($5.67 \times 10^{-8} \text{ W}/(\text{m}^2 \cdot \text{K}^4)$), and k is then defined as follows:

$$k = \frac{16\sigma T_3^3}{3(\alpha + s + 1/\text{WGAP})} \quad (12)$$

In Eq. (12), WGAP is the distance between the adjacent walls. PHOENICS encyclopedia provides a detailed calculation for WGAP. The radiation emissivity of the building walls and the surfaces in the domain has significant impact on the urban thermal environment. Therefore, this study used the field measurement results to consider emissivity value of 0.9 for building walls, 0.92 for concrete covered ground

surfaces, 0.94 for grass covered ground surfaces, and 0.95 for side and top surfaces of the domain.

The vegetation around buildings obstructs the airflow and that phenomenon can be accounted for with the permeability of porous media. Previous studies used an indicator, pore volume fraction that varies from 93% to 99%, to represent the porosity of actual vegetation (Gromke and Ruck 2008, 2009; Gross 1987; Salim et al. 2011). Based on these studies and the dense vegetation distribution for the modeled urban neighborhood, this study used 90% to 97% as the vegetation porosity. Overall, the vegetation model neglected the evapotranspiration and used porosity model as the study focus was on the convective heat transfer.

6 Energy simulation setup for validation

This study created an OpenStudio/EnergyPlus model for Building A to analyze the influence of different external surface CHTC correlations on the heating energy demand for this building. The model is calibrated with actual building electricity and steam consumptions to meet monthly Coefficient of Variation of the Root Mean Square Error (CVRMSE) and Normalized Mean Bias Error (NMBE) requirements defined in ASHRAE Guideline 14-2012 (ASHRAE 2002). The energy model used Actual Meteorological Year (AMY) weather data.

6.1 Description of the energy simulation model

Building A used baseboard heater to meet the space heating demand in winter, and some of the spaces used Package Terminal Air Conditioner (PTAC) for the space cooling demand in summer. This study applied OpenStudio v1.2.4 (OpenStudio 2013) and EnergyPlus v8.0 (EnergyPlus 2012) to create the building geometry, assign thermal boundary conditions, assign the convective baseboard and PTAC systems, and select different CHTC correlations. The Mid-rise apartment templates from the Building Component Library (BCL) (Building Component Library 2012) were used as the baseline for the energy model inputs. CBECS pre-1980 construction sets were used to assign the thermal properties of the building envelope. Throughout the calibration process, the lighting, occupancy, equipment densities and schedules as well as the cooling and heating set-points were modified based on the electricity use patterns to meet the actual building performance (Heidarnejad 2014).

6.2 CHTC correlations setup in EnergyPlus

This study selected three commonly used CHTC algorithms, including DOE-2, TARP, and MoWiTT, in the EnergyPlus program (EnergyPlus 2012). Detailed correlations and

information for these three CHTC algorithms can be found in the EnergyPlus Engineering Reference (Energyplus Engineering Reference 2012). In this study, the forced CHTC correlations for external building surfaces with $\lambda_p = 0.04, 0.11$ and 0.25 were implemented in the EnergyPlus program. The natural convection part employed the existing ASHRAE vertical wall and stable horizontal correlations in the EnergyPlus program. These new CHCT correlations were abbreviated as CHTC0.04, CHTC0.11 and CHTC0.25. To reduce the sudden jump or drop when the wind direction is around 100 degrees from the normal incidence (Yi and Feng 2013), this study employed the correlations for windward, leeward and lateral surface. The adaptive convection algorithm structure in the EnergyPlus program was utilized to combine CHTC correlations for natural convection and forced convection (Beausoleil-Morrison 2000).

7 Results and discussions

The simulation results for the actual urban thermal environment include analyses of the airflow field around multiple buildings and the comparisons of airflow temperature around buildings. These comparisons enable indirect validation of CHTCs. A comparison between the metered space heating and simulated data using different CHTC correlations for 2011 was also made to show the importance of CHTCs when taking into account the actual surrounding environment.

7.1 Flow field around multiple buildings

Due to the lack of measured velocity data, the simulated velocities were not validated with the measured data. However, in order to indicate the difference in thermal boundary conditions, this study also employed the thermal environment simulation with commonly used wall function. Differing from the validation method explained above, which specified the CHTCs at the building walls, this simulation used the general log-law wall function to calculate convective heat transfer adjacent to building walls (PHOENICS 2010). In order to clarify these two different types of simulations, these two simulation scenarios have names defined as the fixed CHTC (FC) case and the wall function (WF) case.

Figure 9 shows the simulated velocity contours and vectors for the FC case and WF case at the height of 1.7 m in the actual urban area. For the FC case shown in Fig. 9(a), the wind velocities at the pedestrian level (1.7 m) around the buildings varied significantly. The air velocity at the incoming airflow impingement zone appeared slightly low, with an approximate range of 0.4 m/s to 1.2 m/s. Similarly, the air velocities at the recirculation zone behind these buildings were around 0.8 m/s. However, the zones between

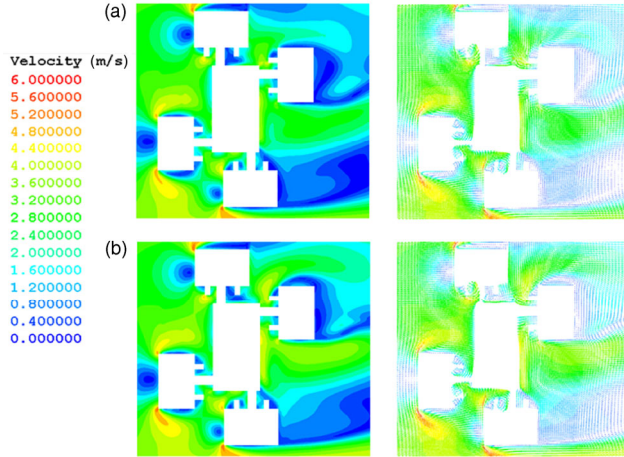


Fig. 9 Horizontal velocity contour and vector distributions at the elevation of 1.7 m for (a) FC case, and (b) WF case

two adjacent buildings showed slightly higher air velocities, roughly ranging from 0.8 m/s to 2.0 m/s. The above phenomena were also present at the height of 1.7 m for the WF case as shown in Fig. 9(b). This velocity increase was mainly due to the fact that the wind direction upstream was perpendicular to the building windward surface, and the majority of wind passed at the lateral sides of the building. Although Building E with the height of 3.5 m decreased the velocity to some extent, the wind effect still had an impact on pedestrian comfort due to the strong wind velocity. Fortunately, the corridors that interconnect the buildings are sealed, so the pedestrians could use the corridors to avoid the exposure to high wind velocities.

In order to describe the velocity distributions adjacent to building wall in more detail, Fig. 10 shows the simulated velocity magnitude close to the center of windward and leeward surfaces in Building D at three different distances from these walls (0.4 m, 1.0 m and 3.0 m for windward surface, 0.5 m, 1.0 m and 3.0 m for leeward surface) for

both the FC case and WF case. In the windward vertical wall, relatively better agreements with the measured data were obtained for both of these cases. However, there were slightly larger discrepancies behind the leeward vertical wall. The results for the wind speed at the distances of 0.5 m and 1.0 m had slight variance, with an averaged relative difference of 1 m/s from 0 m to 25 m. For the distance of 3.0 m, the results for wind speed showed a relatively smaller discrepancy, with the relative difference of around 0.5 m/s from 0 m to 25 m, especially at the higher elevations (>15 m). Note that compared to specified CHTC values in the wall boundary conditions, the wall function overestimated the CHTC, resulting in higher energy losses and a hotter outdoor environment. Therefore, for the same physical model conditions and computational errors, these discrepancies of velocity magnitude between the FC case and WF case are due to different local buoyancy force strengths induced by the temperature difference close to the building wall. However, it should also be pointed that this wall function with larger y^+ values used relatively larger wall-adjacent cells to reduce required computational resources. These wall functions may produce a strong local buoyancy effect adjacent to the building wall to further result in a local increase of air temperatures.

7.2 Comparisons of air temperature around buildings

Figure 11 shows the horizontal temperature distributions at the three different elevations including 2.0 m, 4.0 m, and 6.0 m. Note that the temperature around Buildings A and B, especially at the area close to the windward surface and lateral surface, is lower than that at the upstream flow. This is due to the temperature profile at the inlet boundary that is being perturbed in the terrain between the buildings. Taking Building A as an example, by analyzing the vertical and horizontal velocity vectors, Fig. 12 shows that this

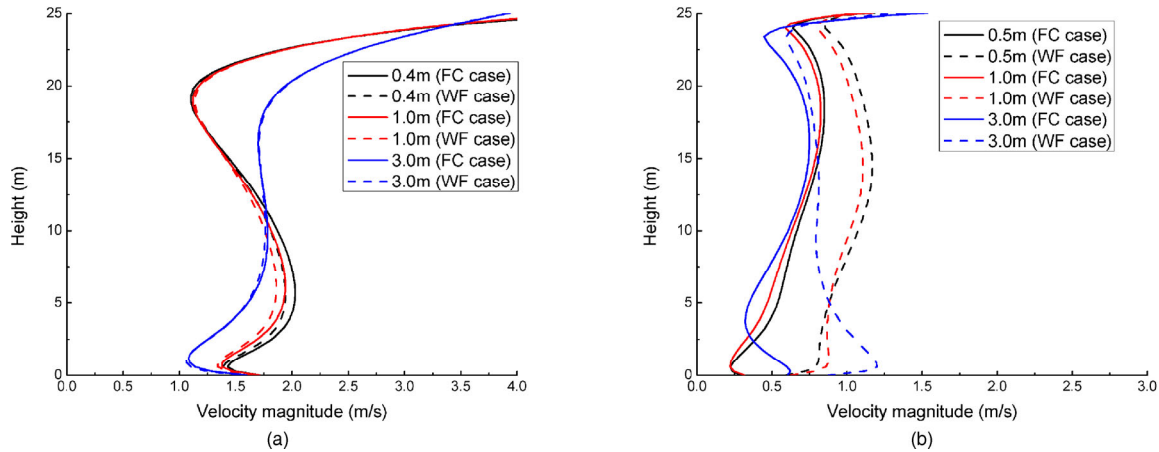


Fig. 10 simulated velocity magnitudes close to (a) windward and (b) leeward surfaces of Building D at three different distances from these walls including 0.4 m (0.5 m for leeward surface), 1.0 m and 3.0 m for the FC case and WF case

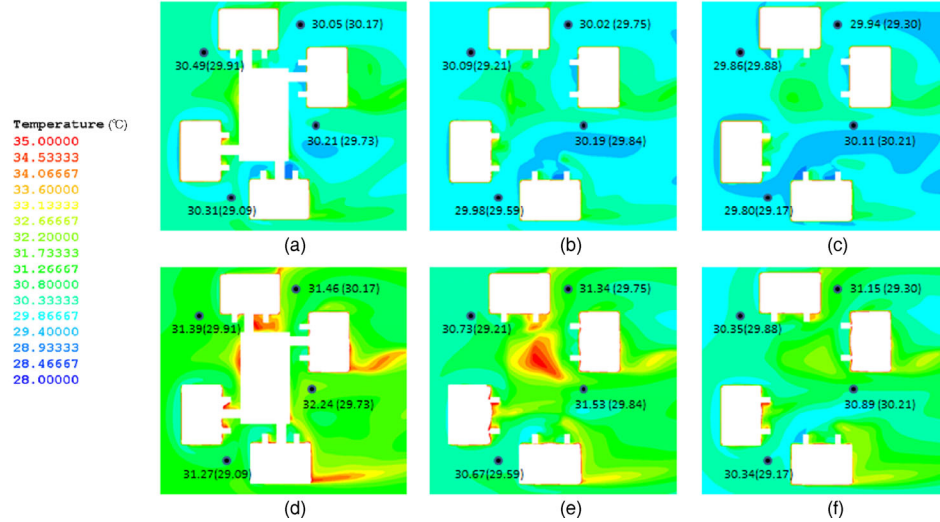


Fig. 11 Horizontal temperature distributions at three different elevations of 2 m, 4 m and 6 m. (a) FC case, 2.0 m, (b) FC case, 4.0 m, (c) FC case, 6.0 m, (d) WF case, 2.0 m, (e) WF case, 4.0 m, (f) WF case, 6.0 m

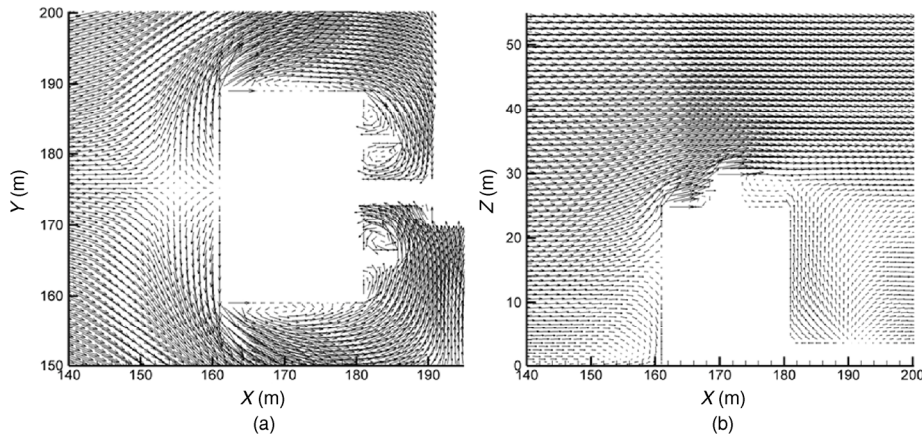


Fig. 12 (a) Vertical and (b) horizontal velocity vectors around Building A

phenomenon was caused by the separation of flow close to the building windward surface. In this case, the stagnation point occurred at about 1/2 of the building height where the flow separates with a portion of air passing upward, some passing sideward and the remainder descending to the lower zone adjacent to the ground. Basically, a small standing vortex close to the ground was generated by descending flow from the stagnation point. In the inlet temperature profile boundary condition, the air temperature decreases with the increase of height. Therefore, the lower temperature flow from the higher elevation had an influence on the thermal environment at the lower elevation, resulting in the phenomena above. In addition, although the velocity upstream was weakened because of the aerodynamic effect of vegetation, it still had a relatively high momentum when impinging on the building windward surface.

The results also showed that the maximum temperature differences between the FC case and field measurement

data were 1.2°C at the elevation of 2.0 m, 0.88°C at the elevation of 4.0 m, and 0.6°C at the elevation of 6.0 m. While the maximum temperature differences between the WF case and field measurement data were 2.5°C, 1.7°C and 1.8°C at three different elevations, respectively. Overall, simulated temperatures using these two methods exhibited relatively larger discrepancies with the field experimental results.

To understand the difference in the results of these two cases, the temperature distributions close to Building D were also examined. For the FC case and WF case, Fig. 13 shows the simulated temperature profiles close to the center of the windward and leeward surfaces of Building D at three different distances including 0.4 m, 1.0 m and 3.0 m for the windward surface, as well as 0.5 m, 1.0 m and 3.0 m for the leeward surface. For the windward surface, the temperature results showed a relatively small variation among these three distances of 0.4 m, 1.0 m, and 3.0 m, with the maximum

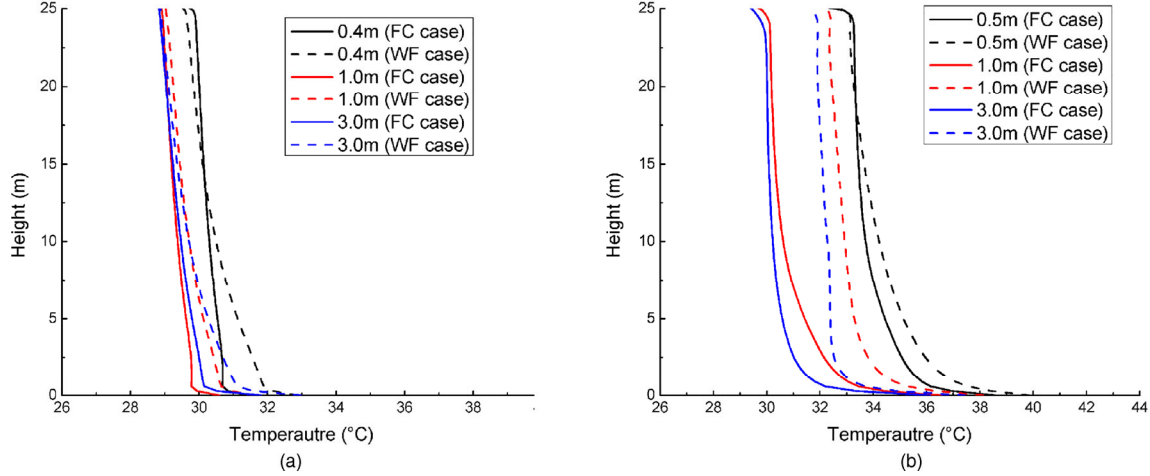


Fig. 13 Simulated temperature profiles close to (a) windward and (b) leeward surfaces of Building D at three different distances from these walls including 0.4 m (0.5 m for leeward surface), 1.0 m and 3.0 m for the FC case and WF case

difference of 1.5°C located in the lower elevation of 0.4 m adjacent to the wall. For the leeward surface, the temperature at the distance of 0.5 m had a small variation with an averaged relative difference of 1.5°C at the area adjacent to the leeward surface in the lower elevation of 0.4 m. For the distance of 1.0 m and 3.0 m, the temperature results showed a relatively larger variation, with the approximately relative difference of 5.5°C and 6°C for 0 m and 25 m, respectively. Therefore, these temperature differences caused a higher buoyancy effect and larger velocities adjacent to the leeward building wall, resulting in higher energy losses and a hotter outdoor environment.

For the FC case and WF case, Fig. 14 shows a comparison between the simulated and measured temperatures at three different elevations including 2.0 m, 4.0 m and 6.0 m. The agreement between the FC case simulation results and the measured air temperatures is very close, and generally within 5%. With this level of agreement between

simulated and measured temperatures, the FC case simulations accurately predicted air temperatures in the actual urban environment. Furthermore, there were relatively larger disagreements between the WF case simulation results and measured data with the relative error of up to 9%. Therefore, the simulated CHTC values derived from the simulations of regular building arrays provided an accurate representation of the convective heat transfer phenomena.

As presented in the literature (Blocken et al. 2009; Defraeye et al. 2010), wall functions can overpredict heat transfer on external building surfaces, as much as 60% compared to low-Reynolds number turbulence models. In this study, the discrepancies between the simulated and measured data may also be partially attributed to the use of the hourly and 15-minute averaged measured data. Nevertheless, the majority of the inaccurate predictions resulted from CHTCs calculations using the wall functions that can be successfully replaced with the newly-developed CHTCs.

7.3 Energy consumption comparisons

The energy consumption of a building depends on its surrounding environment, so this study quantifies the impact that CHCTs and associated convective heat transfer calculations have on the overall building energy consumption. Figure 15 shows a comparison between the metered and simulated heating energy consumption using different CHTC correlations for 2011. The comparisons first showed that the energy consumptions calculated with different CHTC correlations provide results that differ in the range of 2%–16% for the monthly heating energy consumption, with the maximum difference of up to $\pm 27\%$

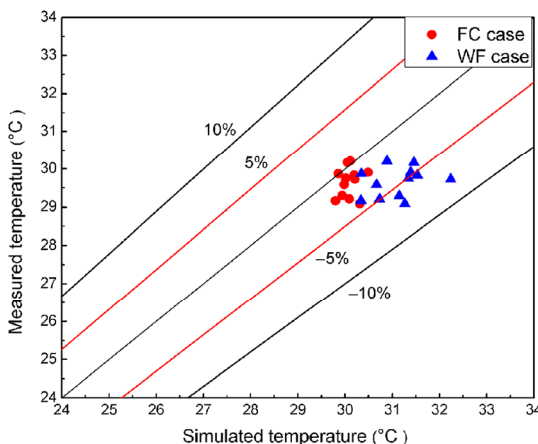


Fig. 14 A comparison between simulated and measured temperature data at all three elevations including 2.0 m, 4.0 m and 6.0 m

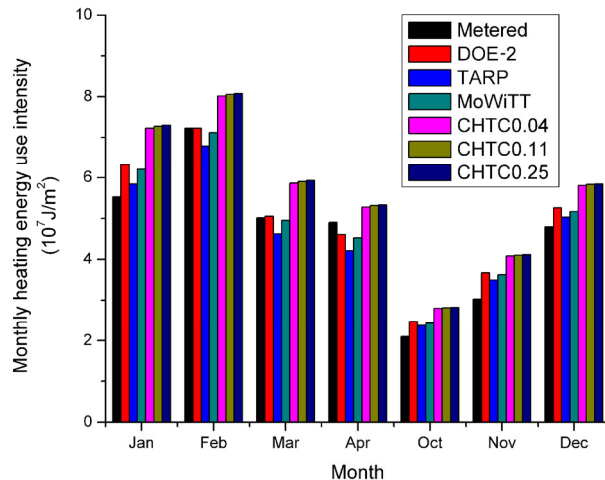


Fig. 15 Monthly heating energy use intensity in 2011 for the case study

in February 2011. Here, the difference between the CHTC correlations based on urban density and default correlations was calculated as Deviation (%) = $(E_{\text{Target}} - E_{\text{Default}})/E_{\text{Default}}$, where the default CHTC correlation was selected to be the DOE-2 correlation for exterior surface in the EnergyPlus program. The new CHTC correlations resulted in an increased heating energy consumption compared to the metered data. This was mainly due to the modified adaptive algorithm that combines the natural and forced convection for windward, leeward, lateral and top surfaces. This algorithm was originally developed and extensively applied to calculate CHTCs for internal building surfaces (Beausoleil-Morrison 2001), so its applicability to the exterior CHTCs was not previously tested. Therefore, a validation is needed to evaluate the applicability of the adaptive algorithm to the external building surfaces.

Interestingly, approximately less than 2% of the variation in the monthly heating energy consumption was observed for CHTC0.04 and CHTC0.25. While this small variation demonstrates that the effect of the new CHTC correlations on the heating energy consumption is negligible even though these correlations take into account the actual building surrounding environment. It should be noted that this relatively small variation in the heating energy consumption is due to different CHTCs associated with the wind sheltering effect and without considering the change in infiltration rates or solar shading. Therefore, further study will include the influence of infiltration rates and solar shading when considering the total energy consumption of a building located in a dense urban neighborhood.

It was also important to note that there were slightly larger discrepancies between the simulated and metered space heating consumptions for January, March and December 2011 as shown in Fig. 15. These discrepancies

indicated that other factors, including (1) adjustment of the temperature set point based on the actual building occupancy, and (2) steam flow rate reduction for the students' winter break, contributed to the actual heating energy consumption. The major discrepancies occur during the students' academic break time periods. For example, during January and December, the metered space heating readings are lower than the simulated results due to the steam flow rate reduction from a typical flow rate due to the students' winter break. Similarly, during March 2011, the metered reading was higher than the simulated energy consumption due to the students' spring break. This study uses adjusted occupancy schedule for March to include the spring break time. Overall, the calibrated energy simulation model met the ASHRAE Guideline 14-2002 requirements to have CVRMSE less than 15% and NMBE less than 5% for the monthly heating consumptions.

8 Conclusions

Accurate assessment of the urban thermal and airflow environment have significant influence on the air pollutant dispersion in the built environment. Specifically, the convective heat transfer coefficients (CHTCs) on the external surfaces of a building are important parameters for accurate numerical simulations of the urban thermal and airflow environment. In this study, a modified "Kato-Launder" version of the $k-\varepsilon$ turbulent (MMK) model was used to simulate actual urban thermal environment. A field measurement was also conducted to provide outdoor thermal environment parameters. The agreement between the simulated and the measured air temperatures is very close, generally within 5%. Consequently, the CFD simulations of air temperatures around the actual urban environment in the present study showed a good performance, and the CHTC values were indirectly validated to provide accurate simulation results. Specifically, to reduce required computational resources, this study benefited from the commonly used wall functions used to validate the simulation results for the actual urban thermal environment. The results showed that the wall function with larger y^+ values slightly overestimated convective heat transfer adjacent to building wall, and less accurately predicted the resultant urban thermal environment.

This study also created a calibrated building energy model for a building located in the urban neighborhood to demonstrate the application of the newly-developed CHTCs. Nevertheless, for the case study building, the CHTC correlations have less than 2% influence on the heating energy consumptions. This indicates that the developed CHTCs with consideration of the wind sheltering effect in

the actual building surrounding environment have more influence on the building exterior surface temperatures, rather than the energy consumption of the building due to the building insulation. Influence of the local urban neighborhood on the energy consumption of the buildings usually requires considerations of other key factors such as the modified infiltration rate, solar shading, in addition to the CHTC correlations.

Overall, this study developed a novel methodology to indirectly validate the CHTC coefficients at the external building surfaces in an actual urban environment with the use of a field measurements and outdoor CFD simulations. The validation shows that the newly-developed CHTCs provide accurate simulations of the outdoor thermal conditions, enabling future studies to accurately simulate the outdoor pollutant dispersion and pedestrian thermal comfort in the actual urban environments.

Acknowledgements

This study is sponsored by the EFRI-1038264 / EFRI-1452045 awards from the National Science Foundation (NSF), Division of Emerging Frontiers in Research and Innovation (EFRI). In addition, the authors would like to thank Yang-Seon Kim and David Tamayo in the Department of Mechanical of The Pennsylvania State University, as well as the Office of Physical Plant (OPP) at The Pennsylvania State University campus especially Michael Prinky and Christopher Yarger.

References

- ASHRAE (2002). ASHRAE Guideline 14-2002. Measurement of Energy and Demand Savings, Atlanta: ASHRAE.
- Awbi HB (1998). Calculation of convective heat transfer coefficients of room surfaces for natural convection. *Energy and Buildings*, 28: 219–227.
- Beausoleil-Morrison I (2000). The adaptive coupling of heat and air flow modeling within dynamic whole-building simulations. PhD Thesis, University of Strathclyde, UK.
- Beausoleil-Morrison I (2001). An algorithm for calculating convection coefficients for internal building surfaces for the case of mixed flow in rooms. *Energy and Buildings*, 33: 351–361.
- Blocken B, Defraeye T, Derome D, Carmeliet J (2009). High-resolution CFD simulations for forced convective heat transfer coefficients at the facade of a low-rise building. *Building and Environment*, 44: 2396–2412.
- Building Component Library (2012). U.S. Department of Energy. Available at <https://bcl.nrel.gov/>.
- Burley BJ (2009). Infiltration mapping for urban environments. PhD Thesis, The Pennsylvania State University, USA.
- Cehlin M, Moshfegh B, Sandberg M (2002). Measurements of air temperatures close to a low-velocity diffuser in displacement ventilation using an infrared camera. *Energy and Buildings*, 34: 687–698.
- Chang H, Kato S, Chikamoto T (2004). Effects of outdoor air conditions on hybrid air conditioning based on task/ambient strategy with natural and mechanical ventilation in office buildings. *Building and Environment*, 39: 153–164.
- Chen H, Ooka R, Harayama K, Kato S, Li X (2004). Study on outdoor thermal environment of apartment block in Shenzhen, China with coupled simulation of convection, radiation and conduction. *Energy and Buildings*, 36: 1247–1258.
- Chen H, Ooka R, Huang H, Tsuchiya T (2009). Study on mitigation measures for outdoor thermal environment on present urban blocks in Tokyo using coupled simulation. *Building and Environment*, 44: 2290–2299.
- Clear RD, Gartland L, Winkelmann FC (2003). An empirical correlation for the outside convective air-film coefficient for horizontal roofs. *Energy and Buildings*, 35: 797–811.
- Davidovic D, Liu J, Heidarnejad M, Srebric J (2014). Airflow study for a cluster of campus buildings using different turbulence modeling approaches. *International Journal of Building, Urban, Interior and Landscape Technology*.
- Defraeye T, Blocken B, Carmeliet J (2010). CFD analysis of convective heat transfer at the surfaces of a cube immersed in a turbulent boundary layer. *International Journal of Heat and Mass Transfer*, 53: 297–308.
- Defraeye T, Blocken B, Carmeliet J (2011). Convective heat transfer coefficients for exterior building surfaces: Existing correlations and CFD modelling. *Energy Conversion and Management*, 52: 512–522.
- Defraeye T, Carmeliet J (2010). A methodology to assess the influence of local wind conditions and building orientation on the convective heat transfer at building surfaces. *Environmental Modelling & Software*, 25: 1813–1824.
- Elnahas MM, Williamson TJ (1997). An improvement of the CTTC model for predicting urban air temperatures. *Energy and Buildings*, 25: 41–49.
- Emmel MG, Abadie MO, Mendes N (2007). New external convective heat transfer coefficient correlations for isolated low-rise buildings. *Energy and Buildings*, 39: 335–342.
- EnergyPlus (2012). U.S. Department of Energy. Available at <http://www.energyplus.gov>.
- Energyplus Engineering Reference (2012). U.S. Department of Energy. Available at <http://www.energyplus.gov>.
- Farea TG, Ossen DR, Alkaff S, Kotani H (2015). CFD modeling for natural ventilation in a lightwell connected to outdoor through horizontal voids. *Energy and Buildings*, 86: 502–513.
- Fitzgerald WB, Fahmy M, Smith IJ, Carruthers MA, Carson BR, Sun Z, Bassett MR (2011). An assessment of roof space solar gains in a temperate maritime climate. *Energy and Buildings*, 43: 1580–1588.
- FLIR Systems (2013). FLIR E series datasheet. Available at <http://www.flir.com/>.
- Fokaides PA, Kalogirou SA (2011). Application of infrared thermography for the determination of the overall heat transfer coefficient (*U*-Value) in building envelopes. *Applied Energy*, 88: 4358–4365.

- Franke J, Hellsten A, Schellen H, Carrissimo B (2007). Best practice guideline for the CFD simulation of flows in the urban environment. COST Action 732: Quality assurance and improvement of microscale meteorological models.
- Grimm NB, Faeth SH, Golubiewski NE, Redman CL, Wu JG, Bai XM, Briggs JM (2008). Global change and the ecology of cities. *Science*, 319: 756–760.
- Gromke C, Blocken B, Janssen W, Merema B, van Hooff T, Timmermans H (2015). CFD analysis of transpirational cooling by vegetation: Case study for specific meteorological conditions during a heat wave in Arnhem, Netherlands. *Building and Environment*, 83: 11–26.
- Gromke C, Ruck B (2008). Aerodynamic modelling of trees for small-scale wind tunnel studies. *Forestry*, 81: 243–258.
- Gromke C, Ruck B (2009). On the impact of trees on dispersion processes of traffic emissions in street canyons. *Boundary-Layer Meteorology*, 131: 19–34.
- Gross G (1987). A numerical study of the air-flow within and around a single tree. *Boundary-Layer Meteorology*, 40: 311–327.
- Haghishat F, Mirzaei P (2011). Impact of non-uniform urban surface temperature on pollution dispersion in urban areas. *Building Simulation*, 4: 227–244.
- Hagishima A, Tanimoto J (2003). Field measurements for estimating the convective heat transfer coefficient at building surfaces. *Building and Environment*, 38: 873–881.
- Hefny MM, Ooka R (2009). CFD analysis of pollutant dispersion around buildings: Effect of cell geometry. *Building and Environment*, 44: 1699–1706.
- Heidarinejad M (2014). Relative significance of heat transfer processes to quantify tradeoffs between complexity and accuracy of energy simulations with a building energy use patterns classification. PhD Thesis, The Pennsylvania State University.
- Hilmer S, Algar D, Neck D, Schleucher E (2010). Remote sensing of physiological data: Impact of long term captivity on body temperature variation of the feral cat (*Felis catus*) in Australia, recorded via Thermochron iButtons. *Journal of Thermal Biology*, 35: 205–210.
- Holden ZA, Abatzoglou JT, Luce CH, Baggett LS (2011). Empirical downscaling of daily minimum air temperature at very fine resolutions in complex terrain. *Agricultural and Forest Meteorology*, 151: 1066–1073.
- Hong B, Lin B (2014). Numerical study of the influences of different patterns of the building and green space on micro-scale outdoor thermal comfort and indoor natural ventilation. *Building Simulation*, 7: 525–536.
- Hong B, Lin B (2015). Numerical studies of the outdoor wind environment and thermal comfort at pedestrian level in housing blocks with different building layout patterns and trees arrangement. *Renewable Energy*, 73: 18–27.
- Hoyano A, Asano K, Kanamaru T (1999). Analysis of the sensible heat flux from the exterior surface of buildings using time sequential thermography. *Atmospheric Environment*, 33: 3941–3951.
- Huang H, Ooka R, Kato S (2005). Urban thermal environment measurements and numerical simulation for an actual complex urban area covering a large district heating and cooling system in summer. *Atmospheric Environment*, 39: 6362–6375.
- Huang SH, Li QS, Xu SL (2007). Numerical evaluation of wind effects on a tall steel building by CFD. *Journal of Constructional Steel Research*, 63: 612–627.
- Kato M, Launder BE (1993). The modeling of turbulent flow around stationary and vibrating square cylinders. In: Proceedings of 9th Symposium on Turbulent Shear Flow, Kyoto, Japan.
- Kim MK, Kim S (2011). Quantitative estimates of warming by urbanization in South Korea over the past 55 years (1954–2008). *Atmospheric Environment*, 45: 5778–5783.
- Lichtenbelt WDV, Daanen HAM, Wouters L, Fronczeck R (2006). Evaluation of wireless determination of skin temperature using iButtons. *Physiology & Behavior*, 88: 489–497.
- Lin B, Li X, Zhu Y, Qin Y (2008). Numerical simulation studies of the different vegetation patterns' effects on outdoor pedestrian thermal comfort. *Journal of Wind Engineering and Industrial Aerodynamics*, 96: 1707–1718.
- Liu J, Heidarinejad M, Gracik S, Srebric J (2014). The impact of exterior surface convective heat transfer coefficients on the building energy consumption in urban neighborhoods with different plan area densities. *Energy and Buildings*, 86: 449–463.
- Liu J, Srebric J, Yu N (2013a). Numerical simulation of convective heat transfer coefficients at the external surfaces of building arrays immersed in a turbulent boundary layer. *International Journal of Heat and Mass Transfer*, 61: 209–225.
- Liu J, Srebric J, Yu N (2013b). A rapid and reliable numerical simulation method for predictions of outdoor thermal environment in actual urban areas. In: Proceedings of ASME 2013 Summer Heat Transfer Conference (HT 2013), Minneapolis, USA.
- Liu, Y, Harris DJ (2007). Full-scale measurements of convective coefficient on external surface of a low-rise building in sheltered conditions. *Building and Environment*, 42: 2718–2736.
- Loveday DL, Taki AH (1996). Convective heat transfer coefficients at a plane surface on a full-scale building facade. *International Journal of Heat and Mass Transfer*, 39: 1729–1742.
- Macdonald RW (2000). Modelling the mean velocity profile in the urban canopy layer. *Boundary-Layer Meteorology*, 97: 25–45.
- Mattingly GE, Peters EF (1977). Wind and trees—Air infiltration effects on energy in housing. *Journal of Industrial Aerodynamics*, 2: 1–19.
- Maxim Integrated (2013). DS1922L/DS1922T Datasheet. Available at <http://www.maximintegrated.com/en/products/comms/ibutton.html>.
- Meinders ER (1998). Experimental study of heat transfer in turbulent flows over wall-mounted cubes. PhD Thesis, Technische Universiteit Delft, The Netherlands.
- Meinders ER, van der Meer TH, Hanjalic K, Lasance CJM (1997). Application of infrared thermography to the evaluation of local convective heat transfer on arrays of cubical protrusions. *International Journal of Heat and Fluid Flow*, 18: 152–159.
- Mochida A, Lun IYF (2008). Prediction of wind environment and thermal comfort at pedestrian level in urban area. *Journal of Wind Engineering and Industrial Aerodynamics*, 96: 1498–1527.
- Murakami S (1993). Comparison of various turbulence models applied

- to a bluff-body. *Journal of Wind Engineering and Industrial Aerodynamics*, 46–47: 21–36.
- Nakamura H, Igarashi T, Tsutsui T (2001). Fluid flow and local heat transfer around two cubes arranged in tandem on a flat plate turbulent boundary layer. *JSME International Journal Series B: Fluids and Thermal Engineering*, 44: 584–591.
- Nakamura H, Igarashi T, Tsutsui T (2003). Local heat transfer around a wall-mounted cube at 45 degrees to flow in a turbulent boundary layer. *International Journal of Heat and Fluid Flow*, 24: 807–815.
- NOAA (2011). National Oceanic and Atmospheric administration. Available at <http://wl.weather.gov/data/obhistory/KUNV.html>.
- Oke TR (1987). Boundary Layer Climates, 2nd edn. London: Methuen.
- OpenStudio (2013). U.S. Department of Energy. Available at <http://openstudio.nrel.gov/>.
- PHOENICS (2010). PHOENICS Reference Manual. Available at <http://www.cham.co.uk/>.
- Richmond-Bryant J, Isukapalli SS, Vallero DA (2011). Air pollutant retention within a complex of urban street canyons. *Atmospheric Environment*, 45: 7612–7618.
- Roache PJ (1994). Perspective—A method for uniform reporting of grid refinement studies. *ASME Journal of Fluids Engineering*, 116: 405–413.
- Salim SM, Cheah SC, Chan A (2011). Numerical simulation of dispersion in urban street canyons with avenue-like tree plantings: Comparison between RANS and LES. *Building and Environment*, 46: 1735–1746.
- Sarrat C, Lemonsu A, Masson V, Guedalia D (2006). Impact of urban heat island on regional atmospheric pollution. *Atmospheric Environment*, 40: 1743–1758.
- Shao J, Liu J, Zhao J, Zhang W, Sun D, Fu Z (2009). A novel method for full-scale measurement of the external convective heat transfer coefficient for building horizontal roof. *Energy and Buildings*, 41: 840–847.
- Sharples S (1984). Full-scale measurements of convective energy-losses from exterior building surfaces. *Building and Environment*, 19: 31–39.
- Takahashi K, Yoshida H, Tanaka Y, Aotake N, Wang F (2004). Measurement of thermal environment in Kyoto city and its prediction by CFD simulation. *Energy and Buildings*, 36: 771–779.
- Taylor EN, DeNardo DF, Malawy MA (2004). A comparison between point- and semi-continuous sampling for assessing body temperature in a free-ranging ectotherm. *Journal of Thermal Biology*, 29: 91–96.
- Tominaga Y, Mochida A, Murakami S, Sawaki S (2008). Comparison of various revised k -epsilon models and LES applied to flow around a high-rise building model with 1:1:2 shape placed within the surface boundary layer. *Journal of Wind Engineering and Industrial Aerodynamics*, 96: 389–411.
- Toparlar Y, Blocken B, Vos P, van Heijst CJF, Janssen WD, van Hooff T, Montazeri H, Timmermans HJP (2015). CFD simulation and validation of urban microclimate: A case study for Bergpolder Zuid, Rotterdam. *Building and Environment*, 83: 79–90.
- Tsuchiya M, Murakami S, Mochida A, Kondo K, Ishida Y (1997). Development of a new kappa-epsilon model for flow and pressure fields around bluff body. *Journal of Wind Engineering and Industrial Aerodynamics*, 67–68: 169–182.
- Walker IS, Wilson DJ, Forest TW (1996). Wind shadow model for air infiltration sheltering by upwind obstacles. *HVAC&R Research*, 2: 265–283.
- Wang KC, Chiou RT (2006). Local mass/heat transfer from a wall-mounted block in rectangular channel flow. *Heat and Mass Transfer*, 42: 660–670.
- Wijeyesundara NE, Chou BR, Jayamaha SEG (1993). Heat flow through walls under transient rain conditions. *Journal of Building Physics*, 17: 118–141.
- Yamaoka N, Yoshida H, Tanabe M, Yamashita M, Koga T (2008). Simulation study of the influence of different urban canyons element on the canyon thermal environment. *Building Simulation*, 1: 118–128.
- Yi YK, Feng N (2013). Dynamic integration between building energy simulation (BES) and computational fluid dynamics (CFD) simulation for building exterior surface. *Building Simulation*, 6: 297–308.
- Zhao J, Liu J, Sun J (2008). Numerical simulation of the thermal environment of urban street canyon and a design strategy. *Building Simulation*, 1: 261–269.